Heliyon 10 (2024) e38328

Contents lists available at ScienceDirect

Heliyon

journal homepage: www.cell.com/heliyon

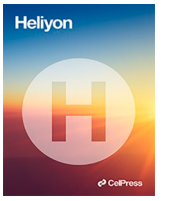

Research article

Construction of Ba-doped Ag_3PO_4/SnO_2 type-II nanocomposites as a promising photocatalyst for boosting photocatalytic degradation of BY28 dye and redox conversion of Cr(VI)/Cr(III)

Zeinab Ghadirian-Arani, Abbas Sadeghzadeh-Attar *, Mohammad Khorasani

Department of Metallurgy and Materials Engineering, University of Kashan, Kashan, P.O. Box 87317-53153, Iran

ARTICLE INFO

Keywords:
Photocatalysis
Ba-doped Ag_3PO_4/SnO_2 nanocomposite
Type II heterojunction
Coupling
Doping

ABSTRACT

In the present study, Ba-doped Ag_3PO_4/SnO_2 type-II heterojunction nanocomposites were fabricated and systemically investigated for the degradation of basic yellow 28 (BY28) dye and Cr(VI) reduction in the photocatalytic process under visible-light irradiation. XRD, XPS, FESEM, DRS, and PL analyses were performed to determine the characterization of synthesized photocatalysts. The optimal 1.5 wt% Ba-doped Ag_3PO_4/SnO_2 nanocomposite exhibited an efficient photocatalytic activity with rate constant of 0.0491 min^{-1} for BY28 degradation and 0.0261 min^{-1} for Cr(VI) reduction, which is 13.3 and 7.5 times higher than that of the SnO_2 nanorods. Such enhanced performance can arise from the one-dimensional structure, extended light absorption toward the visible region, formation of the type II heterojunction, the new defect-related energy states, and efficient charge separation. Furthermore, the photostability of the photocatalysts was studied and a plausible photocatalytic mechanism was proposed.

1. Introduction

Nowadays, rapid global industrialization, consumption of fossil fuels, and increasing energy demand have led to many challenges faced by both human and environmental beings [1]. In particular, environmental pollution originates from the discharge of effluents containing dyes and heavy metals (e.g., Cr(VI), As(V)), which are often difficult to degrade due to their chemically stable and highly toxic nature [2]. It forces humans to move towards environmentally friendly and renewable sources to significantly reduce their harmful environmental impacts. Various approaches are currently applied solely or in combination to eliminate organic dye contaminants and reduction of Cr(VI) to Cr(III) in wastewater including membrane filtration [3], adsorption [4], biodegradation [5], coagulation [6], and photocatalysis processes [7,8].

Heterogeneous photocatalysis as a green and cost-effective technique is a promising process for the removal of pollutants, which can be utilized in the presence of sunlight [9–11]. Semiconductor-based materials due to their unique electronic structure are valuable catalysts for photocatalytic processes. However, the major challenge in this field is to find suitable semiconductors with appropriate band gap, CB and VB energies, which have the best visible-light-driven photocatalytic performance [12]. Among various metal oxide materials, SnO_2 as an n-type semiconductor with the band gap of around 3.6 eV has been widely investigated owing to its nontoxicity, cost-effectiveness, abundance, high electron mobility of ~100–200 $cm^2V^{-1}s^{-1}$, high photostability, and photoactivity [13]. However, due to its wide band gap, it can only be activated by UV light, which covers 3–5% of the solar spectrum [14]. Besides, fast

* Corresponding author.
E-mail address: sadeghzadeh@kashanu.ac.ir (A. Sadeghzadeh-Attar).

https://doi.org/10.1016/j.heliyon.2024.e38328
Received 23 April 2024; Received in revised form 21 September 2024; Accepted 23 September 2024
Available online 24 September 2024

recombination rate of the photogenerated electron/hole pair is other criterion that greatly reduces the catalytic activity of SnO_2 [15]. To alleviate these deficiencies, several strategies have been proposed to increase charge separation and extending the wavelength of photoactivation toward the visible region, such as coupling with other semiconducting materials [16], ion doping [17], sensitization [18], and decorating with noble metal nanoparticles [19].

In recent years, design and construction of hybrid photocatalysts based on the presence of two semiconductors has been developed since effectively promote charge carrier separation, resulting in a high-performance photocatalytic system. In this case, Ag_3PO_4 as a visible light-active material (absorbs at 420–520 nm) with a narrow band gap (2.45 eV) can be a suitable candidate because its quantum efficiency of as high as 90 % is better than that of conventional photocatalysts [20]. For instance, Li et al. [21] designed a heterojunction between SnO_2 and Ag_3PO_4 to enhance the photocatalytic activity of the pristine materials. Although Ag_3PO_4 has excellent photocatalytic properties, it also presents low photostability and high recombination of electron/hole pairs [22]. Nevertheless, the photocatalytic efficiency of Ag_3PO_4 can be appropriately enhanced with electronic structure engineering based on the doping of the Ag_3PO_4 lattice with metal or nonmetal elements. Many studies have been reported to use the dopants into the Ag_3PO_4 lattice such as La [23], Zr [24], Ba [25], Bi [26], w [27], Mn [28]. For example, Yu et al. [25] reported that the doping of Ag_3PO_4 with barium remarkably enhanced the photocatalytic performance where Ba-doped Ag_3PO_4 nanosheets demonstrated a higher photocatalytic performance for degradation of MO and RhB dyes under visible light illumination than the Ag_3PO_4 spherical and cubes particles, respectively. Song et al. [29] introduced the incorporation of nickel into Ag_3PO_4 and exhibited a MO photodegradation of 89 % after 10 min irradiation, which is 4 times larger than pure Ag_3PO_4. Moreover, Amirulsyafiee et al. [24] reported a superior visible light photocatalytic degradation of MO and MB dyes and Cr(VI) photoreduction when compared to Ag_3PO_4. However, the doping ions introduce new energy levels and also brings new recombination centers that act as charge trapping sites and consequently helps in lowering the rate of electron/hole recombination phenomena [22,23].

Motivated by these considerations, herein, we combined the beneficial effects of doping and heterojunction with the aim of constructing ideal catalytic system of Ba-doped Ag_3PO_4/SnO_2 nanocomposite. Thus, the photocatalysts were analyzed in the visible-light-driven degradation of basic yellow 28 (BY28) dye and Cr(VI) photoreduction. The results exhibited that the heterojunction system of Ba-doped Ag_3PO_4/SnO_2 successfully overcomes the limitations of single-component SnO_2 and Ag_3PO_4 due to the synergic effects of accelerated charge separation and enhanced visible-light harvesting.

2. Materials and methods

2.1. Materials and synthesis procedures

All chemicals used in experiments were analytical grade and employed as received without further purification. SnO_2 nanorods were prepared by liquid phase deposition (LPD) [30] using ammonium hexafluorostannate ($(NH_4)_2SnF_6$, Titrachem, 99.99 %) and alumina membrane (AAM, Whatman Co., Anodisc 25, pore size: 100 nm) as the starting materials. In a typical preparation process, the alumina membrane was immersed in the 100 mM aqueous solution of $(NH_4)_2SnF_6$ at room temperature. After 4 h, the membrane was taken out from the treatment solution, rinsed with water and ethanol several times, and then dried for 24 h at room temperature. To achieve the crystalline SnO_2 nanorods, the synthesized samples were calcined at 550 °C for 2 h at a heating rate of 20 °C/min. To remove the alumina membrane, the samples were placed in H_3PO_4 solution for 10 min, and then thoroughly washed with water and ethanol.

In this work, the sol-gel process was used for the synthesis of Ba-doped Ag_3PO_4 nanoparticles [31]. First, an 0.1 mol/L aqueous solution of disodium phosphate (Na_2HPO_4, Sigma-Aldrich, 99 %) was added to the solution of barium nitrate ($Ba(NO_3)_2$, Merck, 99 %) to form $Ba_3(PO_4)_2$. In a cation exchange reaction, the 0.1 mol/L solution of silver nitrate ($Ag(NO_3)$, Merck$\geq$ 99.8 %) was added dropwise to the $Ba_3(PO_4)_2$ solution and stirred magnetically for 2 h to form a yellow suspension. The obtained Ba-doped Ag_3PO_4 was collected, washed with distilled water, and then dried in air for 24 h. Finally, to obtain the crystalline structure, the products were calcined at 450 °C for 1 h at a heating rate of 20 °C/min. For preparing the Ba-doped Ag_3PO_4/SnO_2 nanocomposites with various amounts of Ba dopant, an adequate amount of each semiconductor (with a ratio of 30:70 of Ag_3PO_4:SnO_2) was weighed and then entirely hand-mixed to achieve a homogeneous powder. The samples obtained with various dopants of Ba were labeled as BAS0 (0 wt %), BAS1 (0.5 wt%), BAS2 (1.0 wt%), BAS3 (1.5 wt%), and BAS4 (2.0 wt%), respectively.

2.2. Characterization

The crystal structure of Ba-doped Ag_3PO_4/SnO_2 with different barium amounts (0–2.0 wt%) was analyzed by X-ray diffraction (XRD, Philips X'Pert PRO) with a monochromatic Kα radiation source ($\lambda = 1.542$ °A), under 40 kV and 30 mA. The average crystallite size (D) of Ba-doped Ag_3PO_4 was determined using the Debye-Scherrer's equation [32]: $D = 0.94\lambda/\beta Cos\theta$, where, β is the peak full-width at half-maximum (FWHM), and θ is the Bragg peak position. The (210) plane was selected to estimate the crystallite size. The average lattice parameter (a) of the prepared samples was calculated according to: $a = d.(h^2+k^2+l^2)^{1/2}$, where $d = \lambda/2\sin\theta$ is the (khl) inter-planar spacing. Fourier transform infrared (FTIR) spectroscopy have served to identify the surface functional groups in the synthesized samples using a Nicolet Magna 550 IR spectrometer. The measurements were performed in the transmission mode using KBr pellets at room temperature in the frequency range of 400–4000 cm^{-1}. For the Raman scattering spectra, a Horiba Jobin Yvon spectrometer coupled to with a He-Ne laser source operating at 632.8 nm was used. All spectra were conducted in the region 100-1100 cm^{-1}. To analyze the elemental composition of the synthesized photocatalysts, x-ray photoelectron spectroscopy (XPS) measurements were obtained (Thermo Scientific system) using a monochromatic Al Kα (1486.7 eV) as excitation source. The binding energy of the

elements was referenced to the C1s peak at 284.6 eV from the surface adventitious carbon contamination. The morphology of samples was analyzed by FEG-SEM on a TESCAN instrument (Model MIRA3) operating at 15 kV. To study the optical absorption properties of samples, UV–vis spectra were performed using a V900 spectrophotometer in the wavelength of 200–700 nm. Photoluminescence spectroscopy (PL) was performed using an Agilent G9800 A fluorescence spectrophotometer which was equipped with a xenon lamp. The specific surface area was obtained according to the Brunauer-Emmett-Teller (BET) method via the N_2 adsorption/desorption isotherm by a BELSORP mini II.

2.3. Photocatalytic activity tests

The photocatalytic performance of synthesized photocatalysts was studied by the degradation of BY28 dye and Cr(VI) photoreduction as the representative pollutants at room temperature. The BY28 dye ($C_{21}H_{27}N_3O_5S$, Molecular weight: 433.5 g/mol) was supplied by a textile company without further purification. The reactions were performed in a Pyrex glass photocatalytic reactor containing a suspension of 50 mg sample in 100 mL BY28 solution in an initial concentration of 10 mg/L. Before light irradiation, the solutions were first kept in the dark with magnetic stirring for 40 min to achieve the surface adsorption-desorption equilibrium. The reaction system was then illuminated with a 400 W tungsten lamp equipped with an ultraviolet-cutoff filter, providing visible light $\geq$420 nm. Approximately 5 mL aliquots were collected with a disposable syringe at every 20 min interval and then centrifuged at 4000 rpm for 2 min to completely remove the photocatalysts from the from the photocatalytic reaction system. The concentration of BY28 remaining in the solution at different times was determined using a UV–vis V900 spectrophotometer at the maximum absorbance wavelength of 436 nm. For photocatalytic Cr(VI) reduction, 25 mg of the photocatalyst was added to 50 mL solution containing 50 mg/L potassium dichromate (K_2CrO_4, Sigma-Aldrich) in the initial concentration of 30 mg/L. Similar to photocatalytic dye degradation, the prepared solutions were placed in the dark under constant stirring for 40 min to obtain the surface adsorption-desorption equilibrium. Suspensions were then exposed to visible light for 120 min and 3 mL aliquots were consecutively taken at 20 min intervals and then centrifugated to remove the catalysts. The concentration of Cr(VI) was monitored by the UV–visible spectrometer using diphenylcarbazide colorimetric method at the wavelength of 540 nm, which is free from the H_2O_2 interference [33].

3. Results and discussion

3.1. Morphological studies

Fig. 1 reveals typical FESEM images of the surface morphology of SnO_2 nanorod arrays and Ag_3PO_4/SnO_2 nanocomposite. As shown in Fig. 1(a), SnO_2 arrays have uniformly oriented rod-like structure with an average diameter of about 100 nm similar to that of alumina membrane. Since the dimensions of the nanorods are controlled by the diameter and length of the nanopores, regular nanorods can be fabricated through the LPD process by selecting a proper membrane. When alumina membrane was dipped in the $(NH_4)_2SnF_6$ aqueous solution, a chemical reaction took place between the membrane and tin-based solution, resulting in the formation of metal oxide or hydroxide $(SnF_{6-n}(OH)_n)^{2-}$ in the inner part of membranes pores using the equilibrium reactions of hydrolysis of a metal-fluoro complex ion and consuming of F^- [34]. Fig. 1(b) presents the FESEM image of the synthesized Ag_3PO_4/SnO_2 nanocomposite under the same magnification. It can be seen that the top surface of the SnO_2 nanorod arrays has been deposited a certain amount of Ag_3PO_4 nanoparticles.

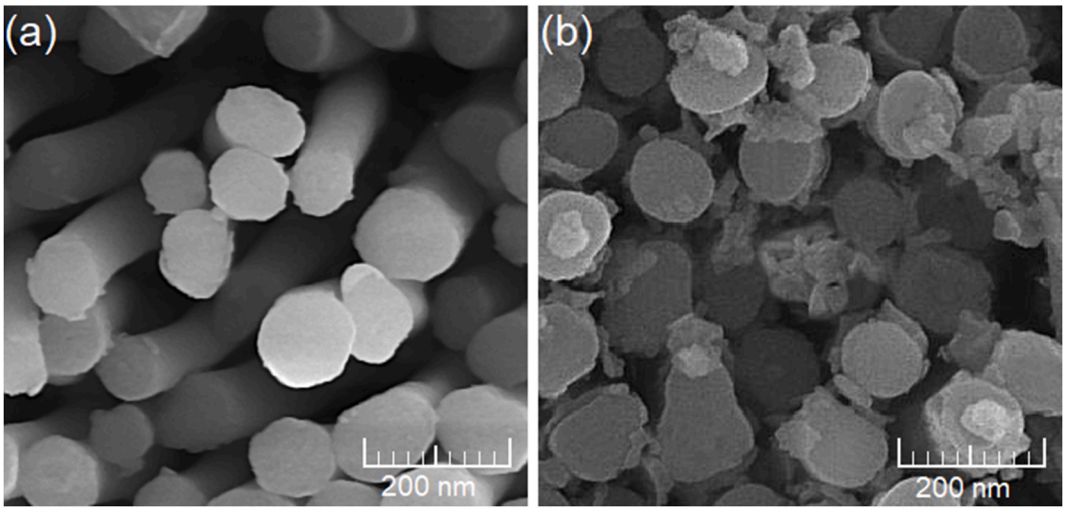

Fig. 1. Surface FESEM images of SnO_2 nanorod arrays and Ag_3PO_4/SnO_2 nanocomposite.

3.2. Structural analysis

The XRD patterns of as-synthesized Ag_3PO_4/SnO_2 and Ba-doped Ag_3PO_4/SnO_2 photocatalysts with different amounts of Ba dopant are shown in Fig. 2. It can be seen that all nanocomposites are composed of cubic Ag_3PO_4 and tetragonal SnO_2 structures. The sharp diffraction peaks at 26.6°, 33.9°, 38°, 51.8°, 54.8°, 61.9°, 64.7°, 65.9° and 78.7° could be indexed as (110), (101), (200), (211), (220), (310), (112), (301), and (321) crystal planes of rutile SnO_2 (JCPDS no.041-1445), demonstrating SnO_2 actually consisted in the Ag_3PO_4/SnO_2 nanocomposites. Several weaker peaks located at 20.9°, 29.7°, 33.4°, 36.6°, and 47.8° are indexed as (110), (200), (210), (211), and (310) planes of Ag_3PO_4, respectively (JCPDS no. 01-084-0511). No other impurities were detected, indicating the products were well-crystallized. As shown in Fig. 3, a shift of the (210) peak towards lower diffraction angles was found with the increase in barium concentration which suggests the fact that Ag^{1+} ions can be uniformly substituted by Ba^{2+} ions in the Ag_3PO_4 lattice. To elucidate the observed peak-shift in the prepared photocatalysts, the mean crystallite size and lattice parameter of Ba-doped Ag_3PO_4 nanoparticles were determined and summarized in Table 1. This shows that the crystallites size of the nanoparticles is in the range of 17.3–43.2 nm and decreases with the increase of Ba content. It was also found that the lattice parameter increases gradually as the Ba doping content in the starting solution increases, mainly due to the ionic radius of Ba^{2+} (1.35 °A) [35] being higher than of Ag^{+} (1.26 °A) [36]. These results reveal that the substitution of Ba into the Ag_3PO_4 lattice slightly increased the unit cell dimension and a lattice distortion occurs.

To provide the further information on the chemical bonding and crystalline structure of the fabricated samples, FTIR spectroscopy and Raman analysis was performed. FTIR spectra of SnO_2, Ag_3PO_4, BAS0, BAS1, BAS2, BAS3, and BAS4 photocatalysts are depicted in Fig. 4(a). All samples presented a broad peak in the region of 3000–3500 cm^{-1} and a peak at 1637 cm^{-1}, which are correspond to OH stretching and deformation vibrations of adsorbed water molecules or surface hydroxyl groups, respectively [37,38]. In the SnO_2 sample, the appearance of broad and strong absorption bands at 535 cm^{-1} and 680 cm^{-1} are due to stretching vibrations of the Sn-O and symmetric vibrations of the O-Sn-O bonds, respectively [39]. In the case of Ag_3PO_4, the characteristic absorption bands of PO_4 groups appeared at 551 cm^{-1} (bending vibration of O-P-O) and 993 cm^{-1} (stretching vibration of P-O bonding) [40]. For the Ba-doped Ag_3PO_4/SnO_2 nanocomposites, the similar peaks both SnO_2 and Ag_3PO_4 components were appeared and only a small shift of the vibrational frequency occurred in the characteristic peaks of Ag_3PO_4 with increasing Ba amount. Moreover, the Ba-O vibration band was detected at 682 cm^{-1} with a low intensity, which proves that Ba was incorporated into the Ag_3PO_4 lattice [41]. The metal-oxygen (M − O) oscillation modes for SnO_2 and Ag_3PO_4 in Ag_3PO_4/SnO_2 and Ba-doped Ag_3PO_4/SnO_2 composites overlap in the range of 500–700 cm^{-1}, although their components can be distinguished. These results suggest that the incorporation of Ba into the Ag_3PO_4

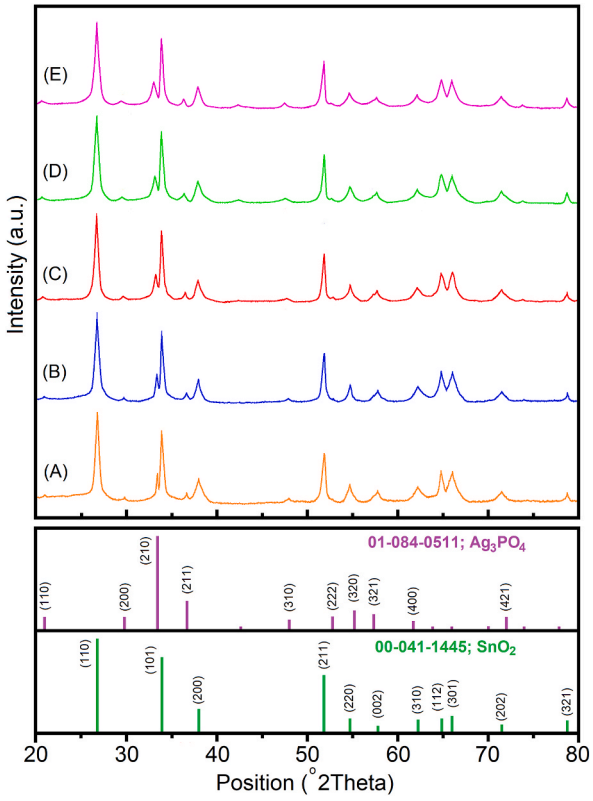

Fig. 2. X-ray diffraction patterns of the Ba-doped Ag_3PO_4/SnO_2 photocatalysts obtained with different contents of Ba dopant: (A) BAS0, (B) BAS1, (C) BAS2, (D) BAS3 and (E) BAS4.

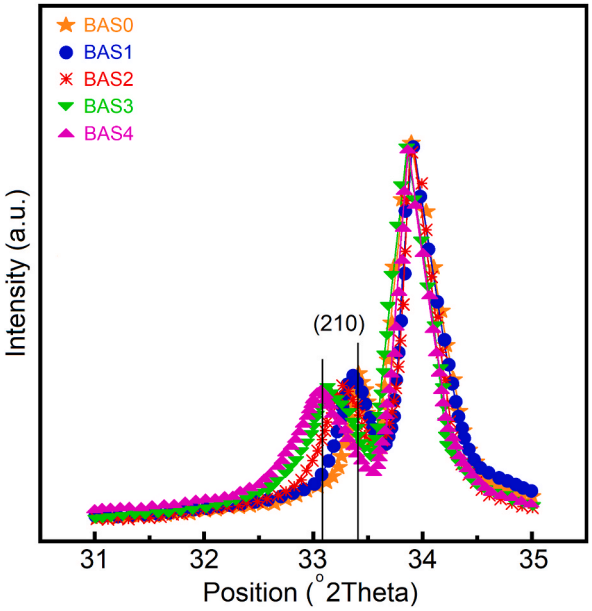

Fig. 3. Angle shift of the (210) plane observed in the XRD patterns of the prepared photocatalysts.

Table 1
Mean crystallite size and lattice parameter for Ba-doped Ag_3PO_4 as a function of barium content.

Ba content (%wt)	0	0.5	1.0	1.5	2.0
Mean crystallite size, D (nm)	43.2	34.7	28.9	21.7	17.3
Lattice parameter, a (°A)	5.998	6.003	6.020	6.045	6.054

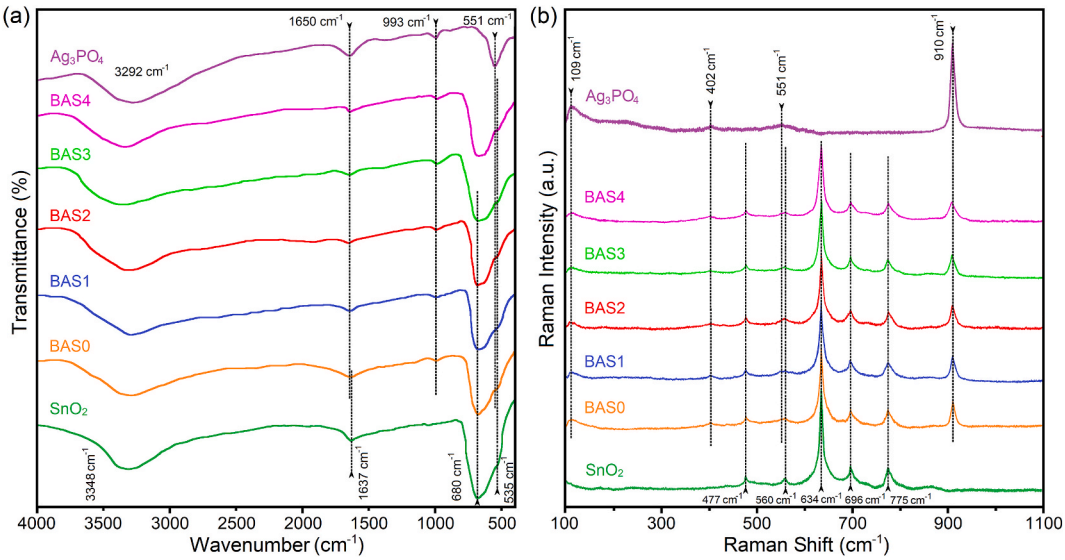

Fig. 4. (a) FTIR and (b) normalized Raman spectra of synthesized SnO_2, Ag_3PO_4, BAS0, BAS1, BAS2, BAS3, and BAS4 photocatalysts.

lattice can increase the affinity of the photocatalyst surface to adsorb water or pollution molecules.

Fig. 4(b) presents the Raman spectra of synthesized SnO_2, Ag_3PO_4, BAS0, BAS1, BAS2, BAS3, and BAS4 photocatalysts. Raman analysis is a highly sensitive tool to detect the local structure and surface defects in solid materials. Raman spectrum of the SnO_2 nanorods indicates five characteristic peaks at 477, 562, 634, 696, and 775 cm^{-1} assigned to the E_{1g}, S1 band, A_{1g}, A_{2u} (LO), and B_{2g} vibrational modes in SnO_2 rutile structure, which is in a good agreement with previous reports [33,42]. On the basis of group

theoryraman, SnO_2 with the rutile lattice generates 18 vibrational modes in the first Brillouin zone canter. These modes is defined as follow [43]:

$$\Gamma = 1A_{1g}+1A_{2g}+1A_{2u}+1B_{1g}+1B_{2g}+2B_{1u}+1E_{1g}+3E_u \quad (1)$$

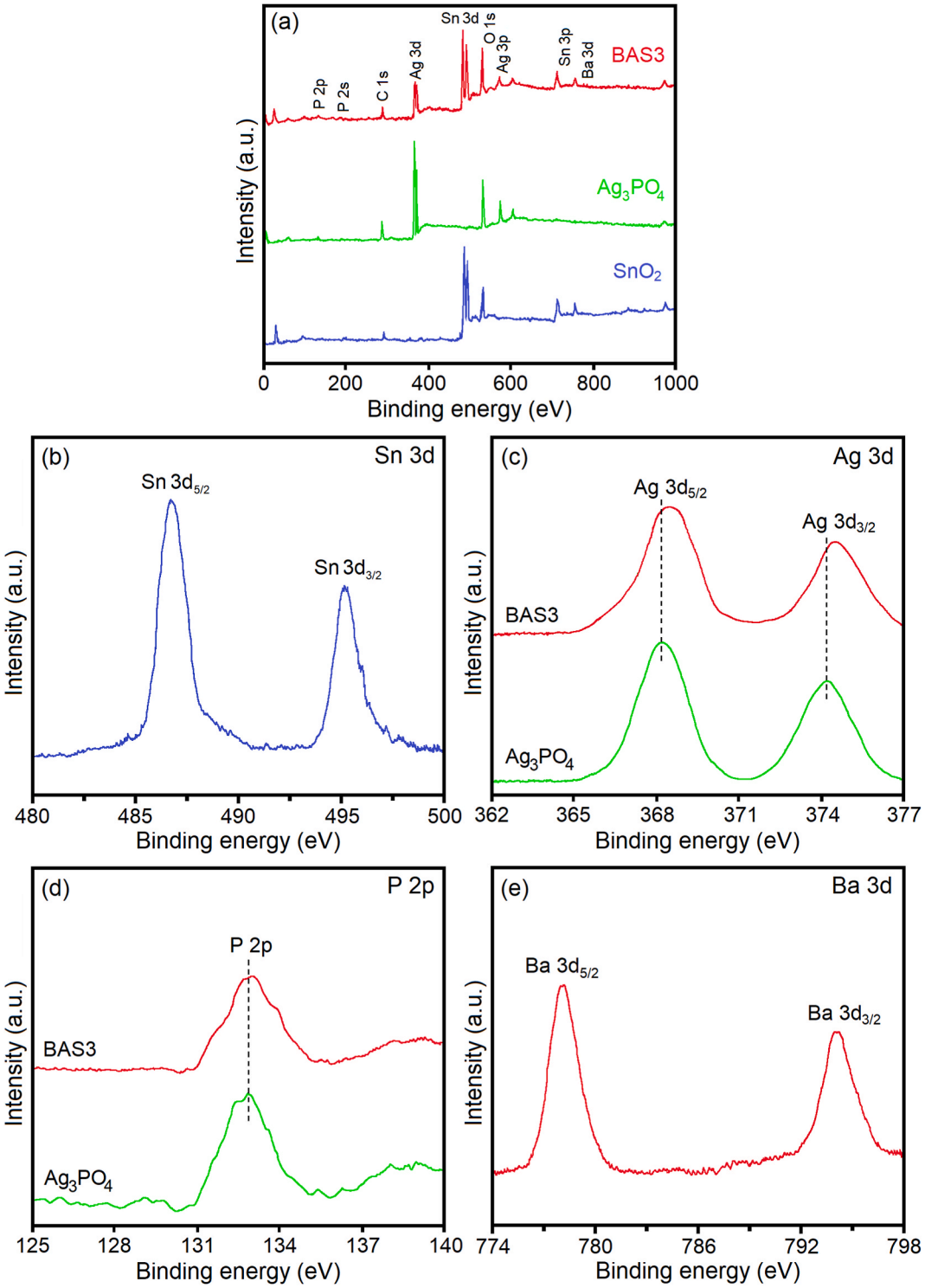

Fig. 5. Spectra of the samples: (a) XPS survey spectra of the Ag_3PO_4 nanoparticles, SnO_2 nanorods and BAS3 nanocomposite, and high-resolution spectra indicating the core level of (b) Sn 3d, (c) Ag 3d, (d) P 2p, and (e) Ba 3d in the BAS3 nanocomposite.

where, the single A_{2u} mode and the triply degenerated E_u modes are IR active, and A_{2g} and $2B_{1u}$ are silent modes. There are four Raman active modes, including three non-degenerated modes of A_{1g}, B_{1g}, B_{2g}, and one doubly-degenerated mode of E_g. The fundamental A_{1g} (634 cm^{-1}) and B_{2g} (775 cm^{-1}) modes are associated with symmetric and asymmetric Sn-O-Sn stretching bonds in the plane perpendicular to the c-axis, while the E_g (477 cm^{-1}) mode vibrates with displacements in the direction of the c-axis [30]. It can be also observed that E_g peak is weak for all the samples, demonstrating the presence of defects/oxygen vacancies in the SnO_2 lattice [43]. For the Ag_3PO_4 nanoparticles, 18 Raman-active modes were expected that only four Raman-active peaks at 109, 402, 551, and 910 cm^{-1} were found due to overlapping and/or weak relative intensity [27]. The intense peak of 910 cm^{-1} can be attributed to the symmetric stretching vibrations of the PO_4 group, while the weak peaks of 551 cm^{-1} and 402 cm^{-1} are associated to the asymmetric and O vibrational bending modes of PO_4, respectively. The band near 109 cm^{-1} may be ascribed to the symmetry vibrational bending mode of Ag-O bonds [44]. In the Ag_3PO_4/SnO_2 nanocomposite, the main characteristic bands of both SnO_2 and Ag_3PO_4 were observed. However, no significant displacement in the position of the peaks was observed. For the Ba-doped Ag_3PO_4/SnO_2 samples, it is found that with increasing the Ba doping content, not only a shift about 0.05–1.5 cm^{-1} in the peak position of the 910 cm^{-1} towards the lower wavenumber is observed, but also the peaks become broaden and weaken. These changes can be attributed to the presence of surface defects and deformation of crystal lattice caused by the introduction of Ba in the Ag_3PO_4 lattice [27]. These results are in a good agreement with the XRD and FTIR results, which both confirm the structural distortion in the Ag_3PO_4 lattice.

XPS experiments was carried out to identify the surface composition and elemental valence states of the synthesized photocatalysts. Fig. 5(a) exhibits the wide-scan XPS spectra of the Ag_3PO_4 nanoparticles, SnO_2 nanorods, and BAS3 nanocomposite, which mainly confirms the presence of Sn, Ag, P, O, C, and a small amount of Ba elements in BAS3 nanocomposite. In addition, no other impurity is detected in the samples. High-resolution XPS spectra for Sn 3d, Ag 3d, P 2p, and Ba 3d are shown in Fig. 5(b–e). The typical XPS spectrum of Sn 3d shown in Fig. 5(b) displays two sharp peaks located at 486.8 and 495.2 eV that can be indexed to Sn $3d_{5/2}$ and Sn $3d_{3/2}$ core level states in SnO_2, respectively [36]. The Ag 3d spectrum of Ag_3PO_4 (Fig. 5(c)) consists of two components at 368.3 and 374.2 eV, which is indexed to the binding energies of Ag $3d_{5/2}$ and $3d_{3/2}$ of Ag^{+} ions, respectively [26]. A slight shift toward lower binding energy was found in the Ag 3d spectrum of the Ba-doped Ag_3PO_4/SnO_2 nanocomposite compared with the undoped Ag_3PO_4 nanoparticles, which has been attributed to the relatively smaller electronegativity of Ba^{2+} compared to Ag^{+1} [25]. With Ba doping, the Ag/P atomic ratio gradually increases, which can be the result of the substitution process of Ag^{+1} by Ba^{2+}. Meanwhile, the spectrum of the P 2p core level region in Fig. 5(d) indicates a characteristic peak at 132.8 eV, corresponding to the oxidation state of P^{5+} [45]. As seen in Fig. 5(e), the two distinct peaks located at 778.1 and 794.0 eV could be related to Ba $3d_{5/2}$ and Ba $3d_{3/2}$ doublet, indicating the presence of the Ba^{2+} state.

3.3. Optical studies

Fig. 6 shows the UV–vis absorptions of Ag_3PO_4, SnO_2, and Ba-doped Ag_3PO_4/SnO_2 with different concentrations of Ba dopant (0, 0.5, 1, 1.5 and 2 wt%). It found that the pristine Ag_3PO_4 revealed an absorption edge at a wavelength of about 515 nm in the visible range, while for the pristine SnO_2 was about 330 nm in the UV range. The absorption edge of Ag_3PO_4/SnO_2 displayed a red shift in optical response upon loading of Ag_3PO_4 onto SnO_2. Compared with those of undoped Ag_3PO_4/SnO_2, the absorption edges of Ba-doped Ag_3PO_4/SnO_2 series photocatalysts slightly shift to a long wavelength with increasing Ba content.

From the UV–visible absorption spectra, $(\alpha h\nu)^{0.5}$ versus photon energy ($h\nu$) was plotted by extrapolating the linear portion of curves to $(\alpha h\nu)^{0.5} = 0$, as observed in Fig. 7. The band gap energy (E_g) of the samples was obtained according to tauc equation [46]:

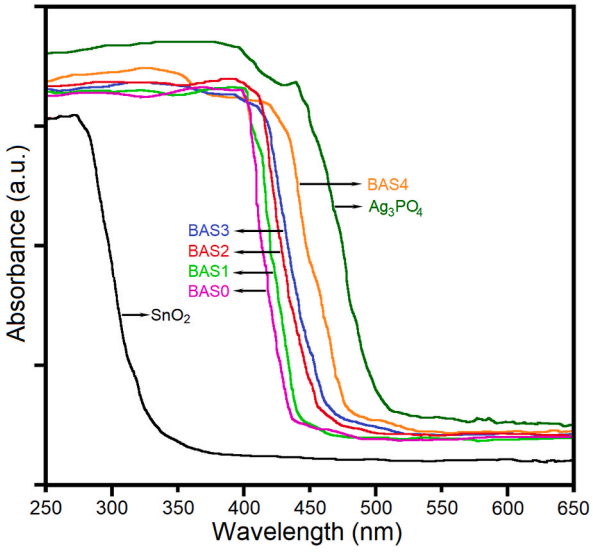

Fig. 6. UV–vis absorption spectra of Ag_3PO_4, SnO_2 and Ba-doped Ag_3PO_4/SnO_2 photocatalysts obtained with different contents of Ba dopant.

$$\alpha h\nu = A(h\nu\text{-}E_g)^2 \quad (2)$$

where α, v, h, and A are the absorption coefficient, the frequency, Plank's constant, and a proportionality constant, respectively. The E_g of Ag_3PO_4, SnO_2, BAS0, BAS1, BAS2, BAS3, and BAS4 samples were estimated as about 2.25, 3.45, 2.68, 2.60, 2.50, 2.48, and 2.40 eV, respectively. The incorporation of Ba into the Ag_3PO_4 lattice gradually reduces the band gap of Ag_3PO_4/SnO_2 composites. Several reports also presented a similar trend that the incorporation of dopant declines the E_g of the Ag_3PO_4 [20,40]. The observed red-shift of the E_g value is due to the introsuction of new energy levels below the conduction band due to the presence of defects, oxygen vacancies, or orbital exchange interactions when Ba^{2+} ions are substituted into the Ag_3PO_4 host lattice.

The room temperature PL was also used to study the transfer and recombination rate of photogenerated electron-hole pair of the synthesized samples. PL spectra of Ag_3PO_4, SnO_2, BAS0, BAS1, BAS2, BAS3, and BAS4 were collected at an excitation wavelength of 325 nm as shown in Fig. 8. The emission spectrum of SnO_2 nanorods exhibited an emission peak at 570 nm, which can be assigned to the surface defects in SnO_2 lattice due to Sn interstitials/O vacancies [46]. The PL spectrum of Ag_3PO_4 nanoparticles showed a broad band centered at 466 nm and a shoulder peak at around 570 nm within the visible light region in accordance with previous work [31]. In comparison with the pristine SnO_2 and Ag_3PO_4, BAS0 displayed lower emission intensity. Generally, a lower PL intensity exhibits a reduction in the recombination rate of electrons and holes, which favors photocatalytic activity [47]. It was also found that the PL intensity of the Ba-doped Ag_3PO_4/SnO_2 photocatalysts decrease as Ba content increased upon 1.5 wt%. Among all synthesized photocatalysts, BAS3 showed the lowest PL intensity. It suggests that the presence of Ba dopant in the Ag_3PO_4 lattice induces surface defects, which helps in trapping the photogenerated electrons and separating the photogenerated charge carriers. These results indicated that the incorporation of Ba atoms into the Ag_3PO_4 nanoparticles and coupling with SnO_2 nanorods can effectively prevent the recombination of electrons/holes, thus leading to an enhanced photocatalytic activity.

3.4. Photocatalytic activity

Photocatalytic degradation of BY28 dye as well as the Cr(VI) reduction were monitored to evaluate the photocatalytic efficiency of the synthesized photocatalysts under visible light illumination. Fig. 9(a) shows the plot of C/C_0 of BY28 dye solution as a function of the irradiation time (t) by the no catalyst, Ag_3PO_4, SnO_2, BAS0, BAS1, BAS2, BAS3, and BAS4 photocatalysts. It can be clearly seen that as irradiation time continuously increased to 120 min, the concentration of BY28 solution could reach 93.5 %, 40.5 %, 62 %, 16 %, 6.5 %, 4 %, 0.2 %, and 2.5 % for no catalyst, Ag_3PO_4, SnO_2, BAS0, BAS1, BAS2, BAS3, and BAS4 photocatalysts, respectively. Photocatalytic degradation of BY28 dye under 120 min of irradiation is evident, where the absorbance intensity at 436 nm declined with the progress of the photocatalytic reaction, as displayed in Fig. 9(b). Based on the obtained results, all of the Ba-doped Ag_3PO_4/SnO_2 samples showed enhanced photocatalytic activity than Ag_3PO_4 nanoparticles and SnO_2 nanorods, and among them, BAS3 photocatalyst exhibited outstanding photocatalytic performance. Absorption spectra of the BY28 dye solution for BAS3 as the best photocatalyst at different irradiation times were illustrated in Fig. 9(c). It also can be observed that the color disappearance of the BY28 solution was noticeable when the irradiation time is up to 40 min (inset in Fig. 9(c)). To statistically compare photocatalytic efficiency, the pseudo-first-order model ($\ln(C/C_0) = -k_{app}.t$) was applied to quantitatively evaluate, as shown in Fig. 9(d). The order of k_{app} values was found BAS3>BAS4>BAS2>BAS1>BAS0>Ag_3PO_4>SnO_2> no catalyst in turn, which is in accordance with the photocatalytic performance of synthesized photocatalysts. Moreover, BAS3 indicated the highest rate constant of 0.0491 min^{-1} which is almost 7.4 and 13.3 times faster than pristine Ag_3PO_4 nanoparticles (0.0066 min^{-1}) and SnO_2 nanorods (0.0037 min^{-1}), respectively. These

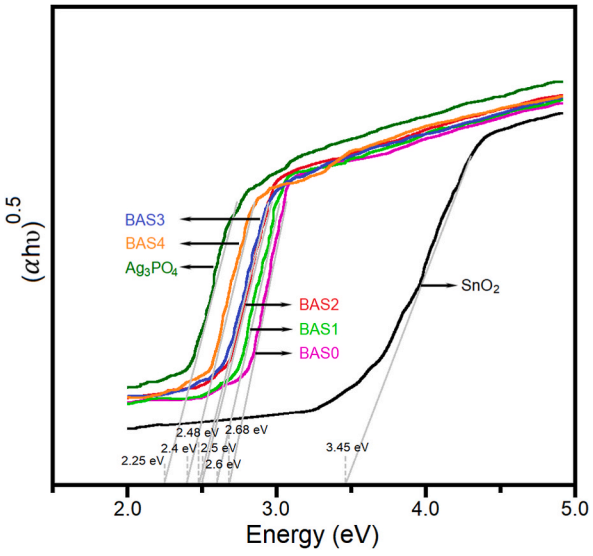

Fig. 7. Estimated band gap of Ag_3PO_4, SnO_2, BAS0, BAS1, BAS2, BAS3, and BAS4 photocatalysts.

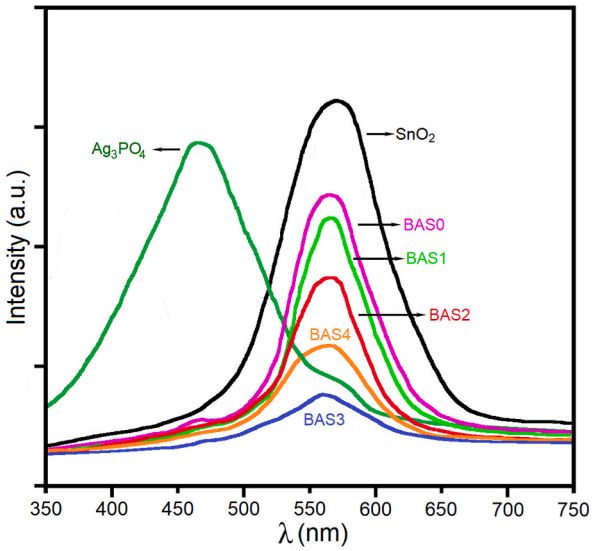

Fig. 8. PL spectra of the synthesized SnO_2, Ag_3PO_4, BAS0, BAS1, BAS2, BAS3, and BAS4 photocatalysts.

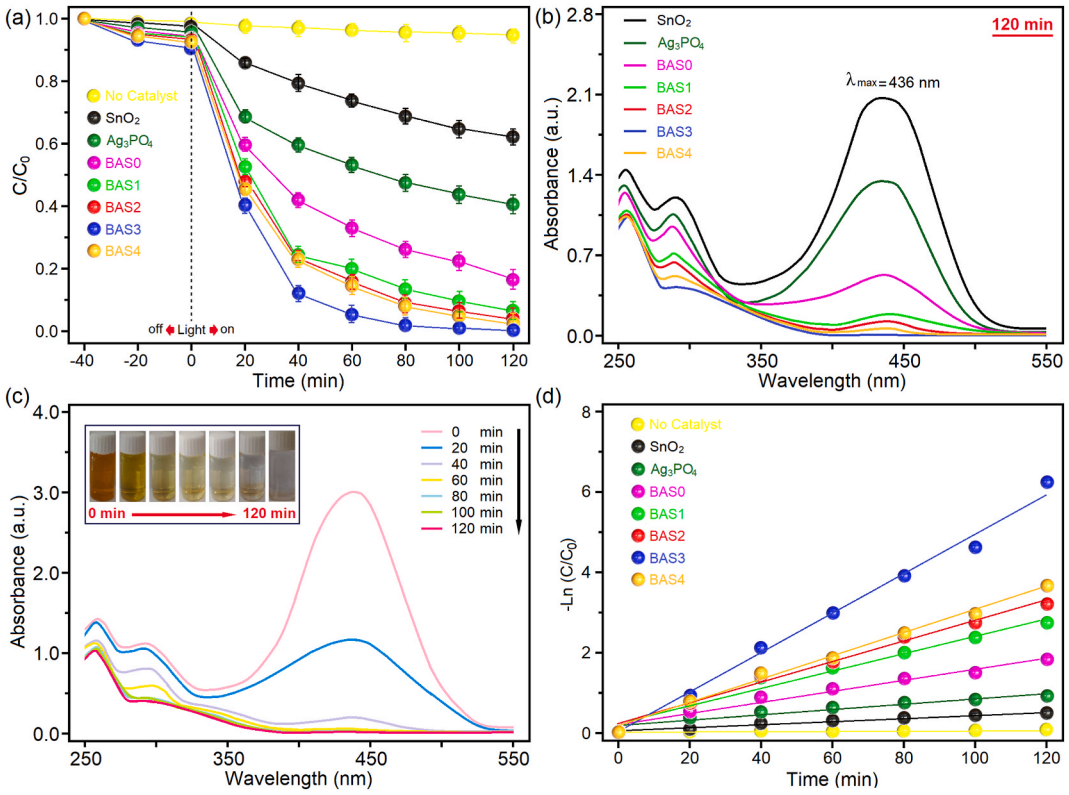

Fig. 9. Photocatalytic activity SnO_2, Ag_3PO_4, and Ba-doped Ag_3PO_4/SnO_2 nanocomposites: (a) plot of (C/C_0) versus t; (b) UV–vis spectra of SnO_2, Ag_3PO_4, BAS0, BAS1, BAS2, BAS3, and BAS4 photocatalysts for the degradation of BY28 dye under 120 min visible-light irradiation (Inset is photographs of these dye solutions), (c) UV–vis spectra of BY28 dye solution after addition of BAS3 photocatalyst (Inset is photographs of these dye solutions), and (d) plot of -Ln (C/C_0) versus t.

results demonstrated that the introduction of Ba into the Ag_3PO_4 lattice and coupling with SnO_2 nanorods, could significantly enhance the photocatalytic activity.

The stability and recycling of the BAS3 photocatalyst were further analyzed for long-term use in practical applications as shown in

Fig. 10(a). The photocatalytic cycling tests were performed under light irradiation, and each run lasted for 120 min. The results showed that after four cycling runs, the BAS3 still possesses a high photocatalytic efficiency, up to 93.5 %, implying that the BAS3 has robust stability and active photocatalytic efficiency for the degradation BY28 dye. To determine the main active species responsible for BY28 degradation, the trapping experiments were carried out for BAS3 photocatalyst under the same conditions as photocatalytic degradation experiments. Isopropanol (IPA), ethylene diamine tetra-acetic acid (EDTA), p-benzoquinone (p-BQ), and were utilized as scavengers for hydroxyl radicals, holes, and superoxide ions, respectively. These scavengers and photocatalyst were added into the BY28 dye solution during 120 min irradiation time. After the addition of scavengers, the degradation performance of BY28 dye decreases. As depicted in Fig. 10(b), it can be found that the addition of p-BQ does slightly slow down the photocatalytic degradation of BY28, whereas the photocatalytic reactions declined drastically with the addition of EDTA and IPA. The pseudo-first order kinetic curves and rate constant are illustrated in Fig. 10(c) and (d). The rate constant values decrease from 0.0491 min^{-1} (without scavenger) to 0.0113 min^{-1} (in the presence of p-BQ), 0.0027 min^{-1} (in the presence of EDTA), and 0.0013 min^{-1} (in the presence of IPA), respectively. These results suggest that $^{\bullet}OH$, h^{+} and $^{\bullet}O_2^{-}$ were all active species, among which $^{\bullet}OH$ and h^{+} are the main active species, which play an important role in the enhanced photocatalytic degradation of BY28.

Apart from photocatalytic degradation BY28 dye, the photocatalytic performance of the prepared photocatalysts was also studied through the redox conversion of Cr(VI) in under 120 min light irradiation. Fig. 11(a) displays the photocatalytic reduction of Cr(VI) without catalyst and over Ag_3PO_4, SnO_2, BAS0, BAS1, BAS2, BAS3, and BAS4 photocatalysts. It can be seen that in the absence of the photocatalyst material, the reduction of Cr(VI) is almost negligible. The photocatalytic reduction efficiency of bare SnO_2 and Ag_3PO_4 in 120 min were only 35 % and 47.2 %, respectively. The photocatalytic efficiency was significantly improved by coupling Ag_3PO_4 and SnO_2, whereas reach to 72.6 %. The data exhibited increase in photocatalytic activity with the increasing Ba dopant amounts up to 1.5 wt%. The reduction of Cr(VI) was found 85.8 %, 89 %, 96 %, and 91 % for BAS1, BAS2, BAS3, and BAS4, respectively. On the other hand, the kinetic of the photocatalytic reactions was investigated and the kinetic data of the Cr(VI) reduction was fitted to a pseudo-

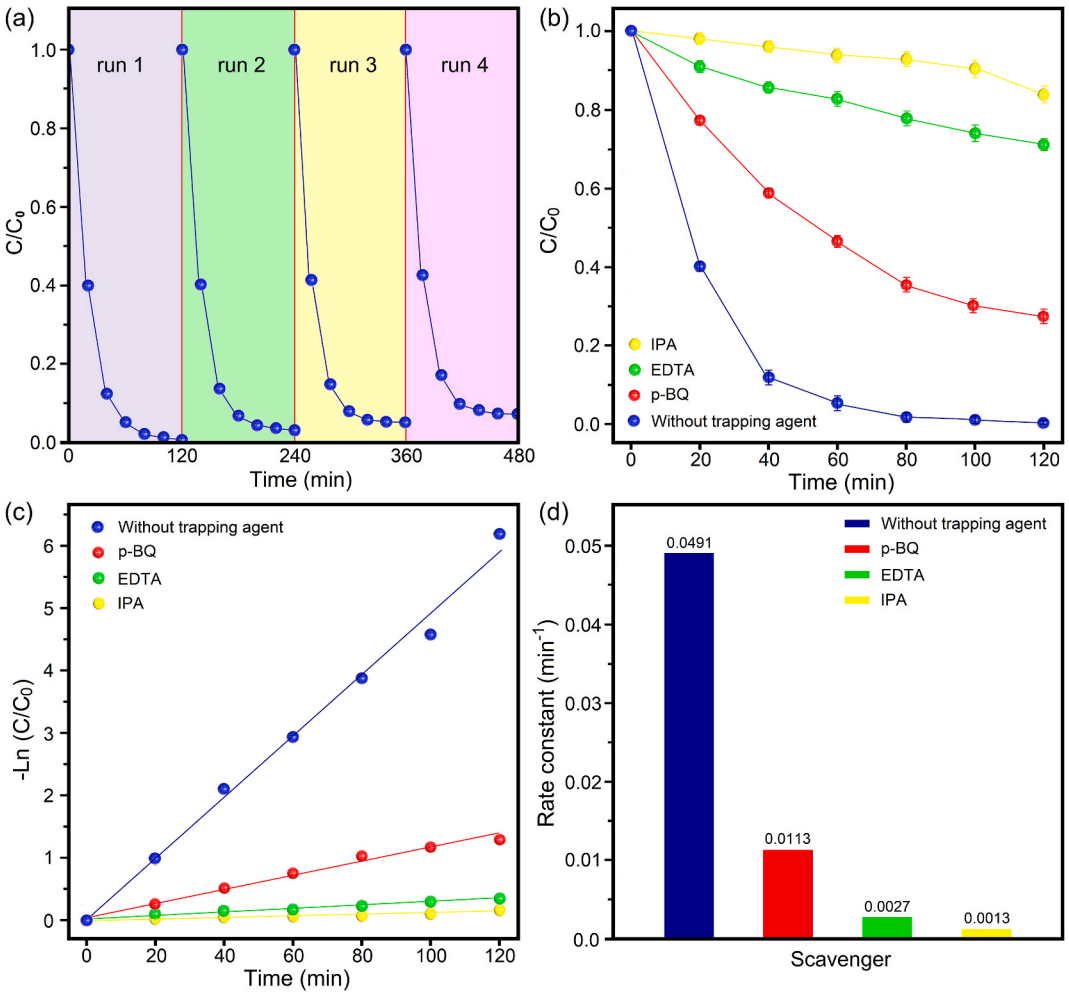

Fig. 10. (a) Stability study, (b) trapping experiment of active species, (c) pseudo-first order kinetic curves, and (d) the kinetic rate constant using p-BQ, EDTA, and IPA on the photocatalytic degradation of BY28 dye solution in the presence of BAS3 photocatalyst under visible-light irradiation.

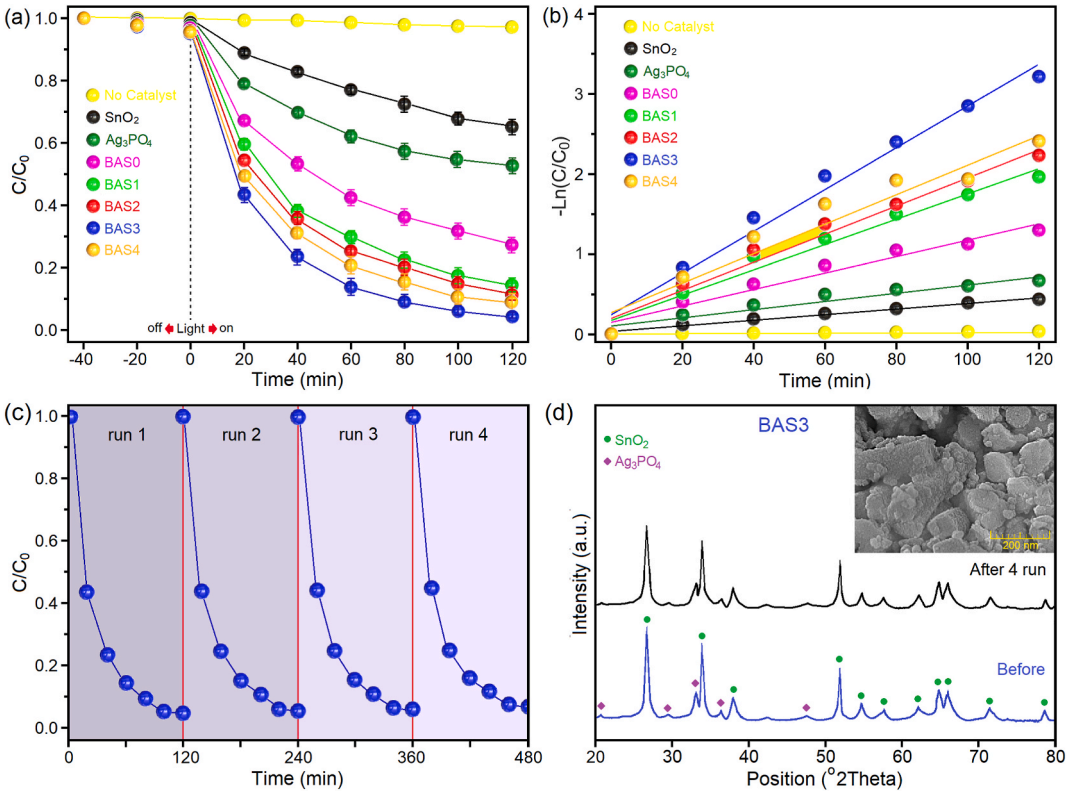

Fig. 11. (a) The plots of (a) C/Co versus time, (b) -Ln (C/C_0) versus t for the photocatalytic redox conversion of Cr(VI)) in absence of the photocatalyst and over SnO_2, Ag_3PO_4, BAS0, BAS1, BAS2, BAS3, and BAS4 photocatalysts under visible-light irradiation, (c) Reusability of BAS3 catalyst for Cr(VI) reduction in four cycles, and (d) XRD patterns of BAS3 photocatalysts before and after four cycling test (inset is the FESEM image of photocatalyst after 4 runs photocatalysis process).

first-order model, as presented in Fig. 11(b). The pseudo-first-order rate constant (k_{app}) was obtained 0.0035, 0.0051, and 0.0102 min^{-1} for SnO_2, Ag_3PO_4, and BAS0 samples, respectively. Among the synthesized photocatalysts in this work, BAS3 is the most effective photocatalyst to reduce Cr(VI) with rate constant of 0.0261 min^{-1}, which is about 7.5 times than that of SnO_2 nanorods, and followed by BAS4 (0.0184 min^{-1}), BAS2 (0.0175 min^{-1}), and BAS1 (0.0158 min^{-1}), respectively. Table 2 summarizes the photocatalytic reduction of Cr(VI) using various SnO_2- and Ag_3PO_4-based photocatalysts. The photostability of BAS3 photocatalyst was evaluated through four consecutive experimental runs of the photoredox conversion of Cr(VI). After each use, the photocatalyst was firstly collected from the reaction medium by centrifugation, followed by washing using deionized water. Recycling data was depicted in Fig. 11(c), the photocatalytic reduction efficiency was found to be 93 % after 4 cycles. The slight decrease in the photocatalyst activity of BAS3 may be related to the adsorption of Cr(III) products onto the catalyst surface or the partial loss of active sites. The results of specific surface area (S_{BET}) to determine the available active sites of BAS3 photocatalyst showed that S_{BET} decreases from 138 m^2/g to 114 m^2/g before and after the four reaction cycles, respectively. However, the high photocatalytic efficiency confirms the stability and reusability of Ba-doped Ag_3PO_4/SnO_2 nanocomposites, demonstrating its feasibility for photocatalytic applications. Furthermore, the stability of BAS3 photocatalyst was evaluated after cyclic regeneration testing using XRD and FESEM analysis, as shown in Fig. 11(d). On the basis of the XRD patterns before and after photocatalysis process and FESEM image (inset) after the four-cycling test, no obvious changes in crystal structure and morphology were observed. It can be seen that only some SnO_2 nanorods were broken after repeating the cyclic tests.

3.5. *Mechanism of photocatalytic activity*

Aforementioned results can help to deduced the mechanism of the enhanced photocatalytic activity of BR46 dye over Ba-doped Ag_3PO_4/SnO_2 nanocomposite. To explain the mechanism, the conduction band (CB) potential and valence band (VB) potential of SnO_2 and Ag_3PO_4 should be considered. The CB and VB potentials of a semiconductor material can be empirically calculated using formula [48]: $E_{CB} = X\text{-}E^e + 1/2\ (E_g)$, and $E_{VB} = X\text{-}E^e\text{-}1/2\ (E_g)$; where E_{CB} and E_{VB} are the potentials of the conduction and valence band edge, E^e is defined the energy of free electrons on the hydrogen scale (4.5 eV), E_g is band gap of the photocatalyst, and X is the geometric mean of electronegativity of constituent atoms, which the X values for SnO_2 and Ag_3PO_4 are 6.25 eV [49] and 5.96 eV [50], respectively, according to the normal hydrogen electrode (NHE). Hence, the E_{VB} and E_{CB} of SnO_2 were determined to be 3.475 eV and 0.025 eV vs. NHE, while those of Ag_3PO_4 were about 2.585 eV and 0.335 eV respectively. It has been known that Ba^{2+} doping into

Table 2
Comparison of reported reaction conditions, including amount of photocatalyst, initial concentration of Cr(VI) solution, light source, and rate constant using SnO_2- or Ag_3PO_4-based catalysts.

Photocatalyst	Amount of Catalyst (mg)	Cr (VI) Concentration (mg/L)	Light Source	Rate constant, k_{app} (min^{-1})	Ref.
Zr-doped Ag_3PO_4	20	50	300 W Xe Lamp (visible light)	0.0076	[20]
La, Zr co-doped Ag_3PO_4	20	50	300 W Xe Lamp (visible light)	0.0074	[24]
Ni-N codoped SnO_2/Fe_2O_3	50	30	300 W Xe lamp ($\lambda \geq 420$ nm)	0.050	[33]
g-C_3N_4/SnS_2/SnO_2	50	50	300 W Xe lamp ($\lambda > 420$ nm)	0.0064	[48]
Ba-doped Ag_3PO_4/SnO_2	25	30	400 W tungsten lamp ($\lambda \geq 420$ nm)	0.0261	This study

Ag_3PO_4 may induce additional mid-gap electronic energy levels just below the conduction band edge. The transition metals dopants can act not only as the temporary photogenerated electron-trapping sites, but also play as shallow capturing sites of photogenerated electrons, thus effectively preventing the recombination of photo-induced carriers, prolonging their lifetime, and improve photocatalytic activity [29,40,51]. Furthermore, Ba doping creates an imbalance of charge in the Ag_3PO_4 lattice, which leads to more OH^- adsorption on the photocatalyst surface to trap more holes, thereby delaying the charge pair recombination and generating more hydroxyl radicals [25]. Both SnO_2 nanorods and Ag_3PO_4 nanoparticles showed low photocatalytic activity under visible-light irradiation, but their composites have presented the good photocatalytic efficiency on the degradation of BY28. Poor photocatalytic efficiency of SnO_2 nanorods is attributed to the weak light absorption response and of Ag_3PO_4 nanoparticles due to high recombination efficiency of the charge carriers and weak light stability [45]. On the other hand, the photo-generated electrons from SnO_2 nanorods or Ag_3PO_4 nanoparticles cannot reduce O_2 to $^{\bullet}O_2^-$ or $^{\bullet}HO_2$, because the standard redox potentials of $O_2/^{\bullet}HO_2 = -0.07$ eV and $O_2/^{\bullet}O_2^- = -0.35$ eV vs. NHE [52] are more negative than the CB edge potential of SnO_2 and Ag_3PO_4.

When SnO_2 nanorods and Ba-doped Ag_3PO_4 nanoparticles were coupled together, Fermi levels (E_f) of two components tend to reach a thermodynamically equilibrium state. Therefore, both the VB and CB of Ag_3PO_4 shift upward beyond the VB and CB of SnO_2 according to type-II band gap configuration. The possible photocatalytic mechanism and charge transfer process of Ba-doped Ag_3PO_4/SnO_2 nanocomposite is schematically shown in Fig. 12. When nanocomposite was irradiated with visible light, the photo-generated electrons in the VB of Ag_3PO_4 are easily excited to the CB with the concomitant generation of holes in the VB. Since the CB edge potential of Ag_3PO_4 is more negative than that of SnO_2, the electrons can transfer to the surface of the of $SrTiO_3$ under the driving force of the energy difference between the CBs of Ag_3PO_4 and SnO_2. Simultaneously, the holes migrate in the opposite direction from VB of SnO_2 to Ag_3PO_4 due to appropriate valence band offsets. These photo-generated electrons and holes react with water and molecular oxygen on the surface of the SnO_2 and Ag_3PO_4 to yield superoxide ($^{\bullet}O_2^-$), hydroxyl ($^{\bullet}OH$) radicals and other active species such as $^{\bullet}HO_2$,

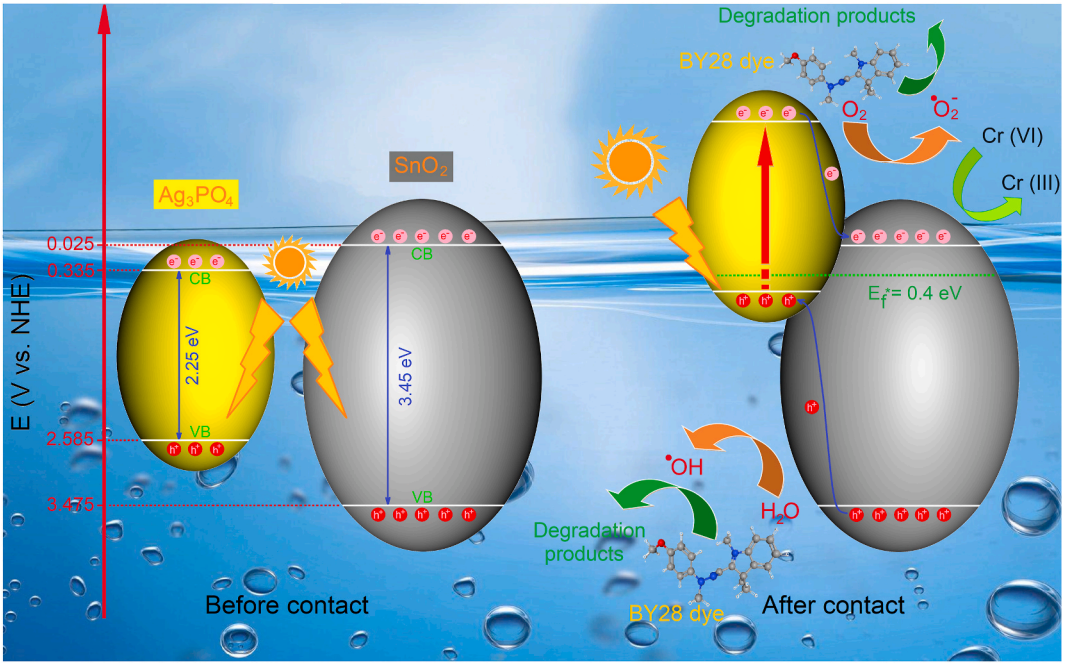

Fig. 12. Schematic diagram of the proposed mechanism, band structure configuration, charge transfer and the charge separation process for the degradation of BY28 dye over Ba-doped Ag_3PO_4/SnO_2 nanocomposite under visible-light irradiation.

which would degrade the BY28 dye. The electrons can be also consumed through a reaction with the molecular oxygen ($O_2+2H^++2e^-\rightarrow H_2O_2$; $H_2O_2+e^-\rightarrow OH^-+{}^{\bullet}OH$) and produce ${}^{\bullet}OH$, which accelerate the degradation process of the dye. Apart from that, in the presence of O_2, Cr(VI) can be directly reduced to Cr(III) by the photoelectrons in the conduction band ($Cr_2O_7^{-2}+14H^++6e^-_{CB}\rightarrow 2Cr^{3+}+7H_2O$) or indirectly by the photogenerated H_2O_2 ($Cr_2O_7^{-2}+8H^++3H_2O_2\rightarrow 2Cr^{3+}+3O_2+7H_2O$), ${}^{\bullet}OOH$ and $O_2^{\bullet-}$. Therefore, an improved charge transfer, efficient charge separation and relatively slow recombination of charge carriers is achieved, resulting in enhanced photocatalytic activity of the Ba-doped Ag_3PO_4/SnO_2 nanocomposite.

4. Conclusion

In this study, we investigated the photocatalytic performance of Ba-doped Ag_3PO_4/SnO_2 heterojunction nanocomposites with different Ba-doping of 0, 0.5, 1, 1.5, and 2 wt% for the degradation of BY28 dye and redox conversion of Cr(VI)/Cr(III) with respect to pristine SnO_2 nanorods or Ag_3PO_4 nanoparticles. The Ba-doped Ag_3PO_4/SnO_2 nanocomposites exhibits excellent activity and stability enabling visible-light-driven dye degradation as well reduction of Cr(VI), although neither component alone is highly efficient. In this sense, the Ag_3PO_4/SnO_2 nanocomposite with 1.5 wt% Ba dopant demonstrated a remarkable enhancement with 99.8 % degradation, which is 61.8 % and 40.3 % greater than that of pristine SnO_2 nanorods and Ag_3PO nanoparticles, respectively. It was also observed to photocatalytic reduce of Cr(VI) with rate constant of 0.0261 min^{-1}, which, which is about 7.5 and 5.1 times than that of SnO_2 and Ag_3PO, respectively. This is basically attributed to the synergistic effects of formed type-II heterojunction between SnO_2 and Ag_3PO_4, and Ba-doping in the Ag_3PO_4 lattice, which facilitate charge transfer, extend visible light absorption and suppress the recombination of charg carriers, leading to the enhanced photocatalytic activity. However, based on the obtained results, we believe that this work can contribute to the development of the design and construction of various photocatalysts and the expansion of their applications in photocatalysis.

CRediT authorship contribution statement

Zeinab Ghadirian-Arani: Writing – original draft, Investigation, Formal analysis. **Abbas Sadeghzadeh-Attar:** Writing – review & editing, Supervision, Conceptualization. **Mohammad Khorasani:** Investigation, Formal analysis.

Declaration of competing interest

The authors declare that they have no known competing financial interests or personal relationships that could have appeared to influence the work reported in this paper.

Acknowledgment

The authors acknowledge the financial support of this study by University of Kashan (159271/09-6).

References

[1] L. Li, F. Tian, L. Qiu, F. Wu, W. Yang, Y. Yu, Recent progress on ruthenium-based electrocatalysts towards the hydrogen evolution reaction, Catalysts 13 (2023) 1497.
[2] H.B. Slama, A.C. Bouket, Z. Pourhassan, F.N. Alenezi, A. Silini, H. Cherif-Silini, T. Oszako, L. Luptakova, P. Golinska, L. Belbahri, Diversity of synthetic dyes from textile industries, discharge impacts and treatment methods, Appl. Sci. 11 (2021) 6255.
[3] E. Pramono, K. Umam, F. Sagita, O.A. Saputr, R. Alfiansyah, R.S.S. Dewi, G.T.M. Kadja, M. Ledyastuti, D. Wahyuningrum, C.L. Radiman, The enhancement of dye filtration performance and antifouling properties in amino-functionalized bentonite/polyvinylidene fluoride mixed matrix membranes, Heliyon 9 (2023) e12823.
[4] X. You, R. Zhou, Y. Zhu, D. Bu, D. Cheng, Adsorption of dyes methyl violet and malachite green from aqueous solution on multi-step modified rice husk powder in single and binary systems: characterization, adsorption behavior and physical interpretations, J. Hazard Mater. 430 (2022) 128445.
[5] R. Alam, R.A. Mahmood, S. Islam, F.C. Ardiati, N.N. Solihat, Md.B. Alam, S.H. Lee, D.H.Y. Yanto, S. Kim, Understanding the biodegradation pathways of azo dyes by immobilized white-rot fungus, Trametes hirsuta D7, using UPLC-PDA-FTICR MS supported by in silico simulations and toxicity assessment, Chemosphere 313 (2023) 137505.
[6] Q. Wei, Y. Zhang, K. Zhang, J.I. Mwasiagi, X. Zhao, C.W.K. Chow, R. Tang, Removal of direct dyes by coagulation: adaptability and mechanism related to the molecular structure, Kor. J. Chem. Eng. 39 (2022) 1850–1862.
[7] X. Wei, P. Wang, H. Fu, C. Zhao, C. Chen Wang, Boosted photocatalytic elimination toward Cr(VI) and organic pollutants over BUC-21/$Cd_{0.5}Zn_{0.5}S$ under LED visible Light, Mater. Res. Bull. 129 (2020) 110903.
[8] Y. Wang, S. Bao, X. Liu, L. Qiu, J. Sheng, W. Yang, Y. Yu, Regulating the peroxymonosulfate activation on N doped δ-MnO_2 nanosheets for tetracycline degradation: N species as the degradation pathways switcher to convert radical to nonradical, Chem. Eng. J. 477 (2023) 147050.
[9] S. Khan, A. Noor, I. Khan, M. Muhammad, M. Sadiq, N. Muhammad, Photocatalytic degradation of organic dyes contaminated aqueous solution using binary $CdTiO_2$ and ternary $NiCdTiO_2$ nanocomposites, Catalysts 13 (2023) 44.
[10] I. Khan, K. Saeed, N. Ali, I. Khan, B. Zhang, M. Sediq, Heterogeneous photodegradation of industrial dyes: an insight to different mechanisms and rate affecting parameters, J. Environ. Chem. Eng. 8 (2020) 104364.
[11] H. Niknam, A. Sadeghzadeh-Attar, Constructing trinary heterostructure of $TiO_2/CoCr_2O_4/SrTiO_3$ to enhance photocatalytic activity toward degradation of yellow 28 dye, Mater. Chem. Phys. 299 (2023) 127489.
[12] W. Navarra, I. Ritacco, O. Sacco, L. Caporaso, M.F. Camellone, V. Venditto, V. Vaiano, Density functional theory study and photocatalytic activity of ZnO/N-doped TiO_2 heterojunctions, J. Phys. Chem. C 126 (2022) 7000–7011.
[13] A. Sadeghzadeh-Attar, Efficient photocatalytic degradation of methylene blue dye by SnO_2 nanotubes synthesized at different calcination temperatures, Sol. Energy Mater. Sol. Cells 183 (2018) 16–24.
[14] R.B. Rajput, R.B. Kale, Hydro/solvothermally synthesized visible light driven modified SnO_2 heterostructure as a photocatalyst for water remediation: a review, Environ. Adv. 5 (2021) 100081.

[15] X. Li, T. Peng, Y. Zhang, Y. Wen, Z. Nan, A new efficient visible-light photocatalyst made of SnO_2 and cyclized polyacrylonitrile, Mater. Res. Bull. 97 (2018) 517–522.
[16] G.N. Silva, T.A. Martins, I.C. Nogueira, R.K. Santos, M.S. Li, E. Longo, G. Botelho, Synthesis of Ag_3PO_4/SnO_2 composite photocatalyst for improvements in photocatalytic activity under visible light, Mater. Sci. Semicond. Process. 135 (2021) 106064.
[17] A. Podurets, M. Khalidova, L. Chistyakova, N. Bobrysheva, M. Osmolowsky, M. Voznesenskiy, O. Osmolovskaya, Experimental and computational study of Ni-doped SnO_2 as a photocatalyst and antibacterial agent for water remediation: the way for a rational design, J. Alloys Compd. 926 (2022) 166950.
[18] K. Michalec, A. Kusior, From Adsorbent to Photocatalyst: the sensitization effect of SnO_2 surface towards dye photodecomposition, Molecules 26 (2021) 7123.
[19] M.J. Fakharian-Qomi, A. Sadeghzadeh-Attar, Template based synthesis of plasmonic Ag-modified TiO_2/SnO_2 nanotubes with enhanced photostability for efficient visible-light photocatalytic H_2 evolution and RhB degradation, ChemistrySelect 5 (2020) 6001–6010.
[20] A. Amirulsyafiee, M.M. Khan, A. Khan, M.Y. Khan, M.H. Harunsani, Influence of Zr doping on Ag_3PO_4 for photocatalytic degradation of dyes and Cr(VI) reduction under visible light irradiation, Mater. Chem. Phys. 291 (2022) 126673.
[21] F. Li, G. Zhang, Y. Song, Preparation and photocatalytic mechanism of Ag_3PO_4/SnO_2 composite photocatalyst, Nano 14 (2019) 1950092.
[22] A. Amirulsyafiee, M.M. Khan, M.H. Harunsani, Ag_3PO_4 and Ag_3PO_4-based visible light active photocatalysts: recent progress, synthesis, and photocatalytic applications, Catal. Commun. 172 (2022) 106556.
[23] A. Amirulsyafiee, M.M. Khan, M.Y. Khan, A. Khan, M.H. Harunsani, Visible light active La-doped Ag_3PO_4 for photocatalytic degradation of dyes and reduction of Cr(VI), Solid State Sci. 131 (2022) 106950.
[24] A. Amirulsyafiee, M.M. Khan, M.Y. Khan, A. Khan, M.H. Harunsani, La, Zr co-doped Ag_3PO_4 for enhanced visible-light photocatalytic degradation of dyes and Cr (VI) photoreduction, Chem. Phys. Impact 5 (2022) 100102.
[25] H. Yu, H. Kang, Z. Jiao, G. Lü, Y. Bi, Tunable photocatalytic selectivity and stability of Ba-doped Ag_3PO_4 hollow nanosheets, Chin. J. Catal. 36 (2015) 1587–1595.
[26] S. Zhang, S. Zhang, L. Song, Super-high activity of Bi^{3+} doped Ag_3PO_4 and enhanced photocatalytic mechanism, Appl. Catal. B Environ. (2014) 129–139.
[27] A.B. Trench, T.R. Machado, A.F. Gouveia, C.C. Foggi, V. Teodoro, I. Sánchez-Montes, M.M. Teixeira, L.G. da Trindade, N. Jacomaci, A. Perrin, C. Perrin, J. M. Aquino, J. André s, E. Longo, Rational design of W-doped Ag_3PO_4 as an efficient antibacterial agent and photocatalyst for organic pollutant degradation, ACS Omega 5 (2020) 23808–23821.
[28] M. Afif, U. Sulaeman, A. Riapanitra, R. Andreas, S. Yin, Use of Mn doping to suppress defect sites in Ag_3PO_4: applications in photocatalysis, Appl. Surf. Sci. 466 (2019) 352–357.
[29] L. Song, Z. Chen, T. Li, S. Zhang, A novel Ni^{2+}-doped Ag_3PO_4 photocatalyst with high photocatalytic activity and enhancement mechanism, Mater. Chem. Phys. 186 (2017) 271–279.
[30] A. Sadeghzadeh-Attar, M.R. Bafandeh, The effect of annealing temperature on the structure and optical properties of well-aligned 1D SnO_2 nanowires synthesized using template-assisted deposition, CrystEngComm 20 (2018) 460–469.
[31] S. Kafian, A. Sadeghzadeh-Attar, Photocatalytic degradation of Basic Blue 41 dye under visible light over $SrTiO_3/Ag_3PO_4$ hetero-nanostructures, Int. J. Appl. Ceram. Technol. 19 (2022) 3347–3357.
[32] P. Debye, P. Scherrer, Interferenzen an regellos orientierten teilchen im röntgenlicht, Phys. Z. 18 (1917) 291–301.
[33] J. Didari, A. Sadeghzadeh-Attar, Ni-N codoped SnO_2/Fe_2O_3 nanocomposite as advanced bifunctional photocatalyst for simultaneous photocatalytic redox conversion of Cr(VI) and As(III), J. Taiwan Inst. Chem. Eng. 119 (2021) 232–244.
[34] A. Sadeghzadeh-Attar, Preparation and enhanced photocatalytic activity of Co/F codoped tin oxide nanotubes/nanowires: a wall thickness-dependence study, Appl. Phys. A 125 (2019) 768.
[35] A. Saito, H. Kagi, S. Marugata, K. Komatsu, D. Enomoto, K. Maruyama, J. Kawano, Incorporation of incompatible strontium and barium ions into calcite ($CaCO_3$) through amorphous calcium carbonate, Minerals 10 (2020) 270.
[36] A. Ahmad, J. Thiel, S. Ismat Shah, Structural effects of niobium and silver doping on titanium dioxide nanoparticles, J. Phys.: Conf. Ser. 61 (2007) 11–15.
[37] H. Selim, E.R. Sheha, R. Elshypany, P. Raynaud, H.H. El-Maghrabi, A.A. Nada, Superior photocatalytic activity of $BaO@Ag_3PO_4$ nanocomposite for dual function degradation of methylene blue and hydrogen production under visible light irradiation, Catalysts 13 (2023) 363.
[38] A. Abrishami-Rad, A. Sadeghzadeh-Attar, Fe-doped $BiVO_4$ photocatalyst assisting SnO_2 nanorod arrays for efficient visible-light-driven degradation of Basic Red 46, J. Taiwan Inst. Chem. Eng. 151 (2023) 105110.
[39] S. Sivakumar, E. Manikandan, Novel synthesis of optical, photoluminescence properties and supercapacitor application on Zn^{2+} doping $Sn_{1-x}Zn_xO_2$ nanoparticles, Int. J. Sci. Res. Phys. Appl. Sci. 6 (2018) 1–13.
[40] H. El Masaoudi, I. Benabdallah, B. Jaber, M. Benaissa, Enhanced visible light photocatalytic activity of Cu^{2+}-doped Ag_3PO_4 nanoparticles, Chem. Phys. 545 (2021) 111133.
[41] M.A. Ansari, N. Jahan, Structural and optical properties of BaO nanoparticles synthesized by facile Co-precipitation method, Materials Highlights 2 (2021) 23–28.
[42] A. Sadeghzadeh-Attar, Binary Zn-doped SnO_2/Al_2O_3 nanotube composites for visible-light-driven photocatalytic degradation of Basic Blue 41, ACS Appl. Nano Mater. 3 (2020) 9931–9942.
[43] S. Mehraj, M.S. Ansari, Alimuddin, Annealed SnO_2 thin films: structural, electrical and their magnetic properties, Thin Solid Films 589 (2015) 57–65.
[44] H. Agbeb, N. Raza, D. Dodoo-Arhin, A. Chauhan, R.V. Kumar, H_2O_2 rejuvenation-mediated synthesis of stable mixed-morphology Ag_3PO_4 photocatalysts, Heliyon 4 (2018) e00599.
[45] M. Liu, G. Wang, P. Xu, Y. Zhu, W. Li, Construction of Ag_3PO_4/SnO_2 heterojunction on carbon cloth with enhanced visible light photocatalytic degradation, Appl. Sci. 10 (2020) 3238.
[46] A. Sadeghzadeh-Attar, I. Akhavan-Safaei, M.R. Bafandeh, UV-visible absorption and photoluminescence characteristics of SnO_2 nano-tube/wire arrays fabricated by LPD method, Int. J. Appl. Ceram. Technol. 15 (2018) 1084–1094.
[47] R.B. Rajput, R.B. Kale, Hydro/solvothermally synthesized visible light driven modified SnO_2 heterostructure as a photocatalyst for water remediation: a review, Environ. Adv. 5 (2021) 100081.
[48] Y. Yang, X.A. Yang, D. Leng, S.B. Lang, W.B. Zhang, Fabrication of $g\text{-}C_3N_4/SnS_2/SnO_2$ nanocomposites for promoting photocatalytic reduction of aqueous Cr(VI) under visible light, Chem. Eng. J. 335 (2017) 491–500.
[49] H. Chen, Y. Hu, Z. Ying, Y. Xia, J. Ye, J. Zhao, S. Zhang, BiOI-SnO_2 heterojunction design to boost visible-light-driven photocatalytic NO purification, Int. J. Environ. Res. Publ. Health 20 (2023) 4009.
[50] J. Su, Y. Fan, Y. Yan, T. Liu, H. Li, Z. Li, F. Song, A one-pot synthesis of $AgBr/Ag_3PO_4$ composite photocatalysts, RSC Adv. 11 (2021) 9865–9873.
[51] X. Li, P. Xu, M. Chen, G. Zeng, D. Wang, F. Chen, W. Tang, C. Chen, C. Zhang, X. Tan, Application of silver phosphate-based photocatalysts: barriers and solutions, Chem. Eng. J. 336 (2019) 339–357.
[52] D.A. Armstrong, R.E. Huie, W.H. Koppenol, S.V. Lymar, G. Merényi, P. Neta, B. Ruscic, D.M. Stanbury, S. Steenken, P. Wardman, Standard electrode potentials involving radicals in aqueous solution: inorganic radicals (IUPAC Technical Report), Pure Appl. Chem. 87 (2015) 1139–1150.